






Ultra-thin GaAs solar cells with nanophotonic metal-dielectric diffraction gratings fabricated with displacement Talbot lithography

Larkin Sayre¹  | Eduardo Camarillo Abad²  | Phoebe Pearce²  | Pierre Chausse³ | Pierre-Marie Coulon³  | Philip Shields³  | Andrew Johnson⁴ | Louise C. Hirst^{1,2} 

¹Department of Materials Science & Metallurgy, University of Cambridge, 27 Charles Babbage Road, Cambridge, CB3 0FS, UK

²Department of Physics, University of Cambridge, Cambridge, CB3 0HE, UK

³Department of Electronic & Electrical Engineering, University of Bath, Bath, BA2 7AY, UK

⁴IQE plc, Pascal Close, St. Mellons, Cardiff, CF3 0LW, UK

Correspondence

Louise C. Hirst, Department of Materials Science & Metallurgy, University of Cambridge, 27 Charles Babbage Road, Cambridge CB3 0FS, UK.
Email: lh619@cam.ac.uk

Funding information

Cambridge Trust; Consejo Nacional de Ciencia y Tecnología; Isaac Newton Trust; H2020 European Research Council, Grant/Award Number: 853365; UK Space Agency, Grant/Award Number: PF2-012; Engineering and Physical Sciences Research Council, Grant/Award Numbers: EP/L015978/1, EP/M015181/1, EP/M022862/1

Abstract

Ultra-thin photovoltaics enable lightweight flexible form factors, suitable for emerging terrestrial applications such as electric vehicle integration. These devices also exhibit intrinsic radiation tolerance and increased specific power and so are uniquely enabling for space power applications, offering longer missions in hostile environments and reduced launch costs. In this work, a GaAs solar cell with an 80-nm absorber is developed with short circuit current exceeding the single pass limit. Integrated light management is employed to compensate for increased photon transmission inherent to ultra-thin absorbers, and efficiency enhancement of 68% over a planar on-wafer equivalent is demonstrated. This is achieved using a wafer-scale technique, displacement Talbot lithography, to fabricate a rear surface nanophotonic grating. Optical simulations definitively confirm Fabry-Perot and waveguide mode contributions to the observed increase in absorption and also demonstrate a pathway to short circuit current of 26 mA/cm², well in excess of the double pass limit.

KEYWORDS

ultra-thin, GaAs, nanophotonic, displacement talbot lithography

1 | INTRODUCTION

The development of thin and ultra-thin photovoltaic devices with integrated light management has been widely studied in recent years, with a view to increasing device performance, achieving lightweight, flexible embodiments for systems integration and reduced materials usage.¹ These devices are also compelling candidates for space power applications as they exhibit intrinsic tolerance to the damaging radiation environments found outside of the Earth's protective atmosphere. Space photovoltaics are bombarded with electron and proton

radiation, which can cause dislocations in the lattice structure of the device active layers, reducing diffusion lengths and degrading charge carrier collection efficiency. The development of photovoltaic devices with greater tolerance to radiation exposure would enable longer on-orbit lifetimes and missions in currently inaccessible high radiation environments, as well as the reduction or elimination of rigid and heavy protective coverglass for lightweight, flexible form factors. Intrinsic radiation tolerance has previously been demonstrated in 80 nm GaAs devices, showing no degradation in short circuit current (J_{SC}) for 3 MeV proton fluence up to 10^{14} cm⁻², while J_{SC} of

This is an open access article under the terms of the Creative Commons Attribution License, which permits use, distribution and reproduction in any medium, provided the original work is properly cited.

© 2021 The Authors. Progress in Photovoltaics: Research and Applications published by John Wiley & Sons Ltd.

comparable 800 nm devices degraded to 26% of the starting value.² The devices in this proof of concept demonstration, however, had poor beginning-of-life performance (AMO J_{SC} =5.62 mA/cm²), primarily because they were processed on-wafer without light management.

As devices are made thinner, high transmission losses resulting in lower J_{SC} become an increasing challenge. This can be addressed with integrated light management architectures to extend the optical path length of incident solar photons, increasing total absorption in the device. These optical systems can take different forms including (i) a rear surface planar mirror to enable a double-pass of the device,^{3,4} (ii) a Lambertian surface to scatter light outside of the optical escape cone at the front surface⁵⁻⁸ and (iii) a nanophotonic array to preferentially scatter light into optical modes supported by the ultra-thin film.^{9,10} Previous studies have made use of techniques including nanoimprint lithography^{10,11} to fabricate GaAs devices with nanostructured back surfaces. Displacement Talbot lithography (DTL) is an emerging photolithographic patterning technique which enables the fabrication of high aspect ratio features over large areas, with feature size down to ~100 nm.¹² Wafers are patterned with a single exposure, making this technique suitable for rapid, large area patterning,¹³ as required for the fabrication of photovoltaic devices. Complex patterns can be created using lateral displacements during exposure or using multiple exposures.¹⁴ As with nanoimprint techniques, DTL requires the fabrication of a mask (or master) by electron beam lithography or interference lithography; however, as DTL is a noncontact method, this mask can be reused an unlimited number of times without degradation. Nanophotonic arrays are fabricated from materials with contrasting refractive index. Metallic systems are particularly promising given their strong scattering of light,¹⁵⁻¹⁷ but they can also exhibit unwanted parasitic absorption.

Another key challenge for ultra-thin devices is achieving good diode performance. Contacting schemes must be carefully designed to avoid the diffusion of Au into the active device layer, which degrades diode performance through the introduction of shunt paths and recombination centres at the junction. Furthermore, surface effects become increasingly important on this length scale, as the diode is fully depleted, and therefore surfaces must be passivated.

Solar energy conversion efficiency of 19.9% under AM1.5G, approximately equivalent to 17.8% under AMO (see Supporting Information for calculation), was recently demonstrated in a GaAs solar cell with an active layer thickness of 205 nm (330 nm including window and back surface field layers).¹⁰ The thinnest possible devices will be required in order to fully benefit from intrinsic radiation tolerance. As an example, in a geostationary orbit an 800 nm GaAs device without coverglass might survive approximately two years, while an 80 nm equivalent would survive more than a decade.¹⁸

In this work, GaAs solar cells with active layer thickness 80 nm (120 nm including window and back surface field layers) are developed, featuring an integrated Ag/SiN nanophotonic grating, patterned using DTL. Highly doped AlGaAs is commonly employed as a p-type passivation layer for ultra-thin GaAs devices^{2,4,10,11} because of its favourable band alignment and lower absorption coefficient, particularly for higher Al compositions; however, the results of this study indicate that InGaP makes a superior p-type barrier demonstrating near ideal passivation of the front surface, with all charge carriers generated in this layer extracted as current and diode performance metrics comparable with much thicker devices. AMO solar energy conversion efficiency of 9.08% is achieved, which is comparable to an equivalent device with a planar Ag mirror. Simulations indicate that the addition of an anti-reflection coating (ARC) and reduction in front contact shading losses, as well as further optimization of the nanophotonic array geometry, would increase the efficiency of the nanophotonic device to 16.0%, while applying the same ARC and front contact shading to the planar Ag device would only increase its efficiency to 14.0%. This highlights the potential for devices with integrated nanophotonic light management to exceed the efficiency of single-pass and double-pass optical designs on this ultra-thin device length scale; however, this is only achieved with precise optimization and in certain cases a rear surface planar mirror can provide equivalent or even more favourable performance. Significantly, this work shows a pathway to improving beginning-of-life efficiency for ultra-thin devices in a regime where intrinsic radiation tolerance has been demonstrated.

Layer	Material	Dopant	Doping density (cm ⁻³)	Thickness (nm)	
				Target	Measured
n-type contact	GaAs	Si	5×10^{18}	300	318
Hole barrier	In _{0.47} AlP	Si	5×10^{18}	20	17
n-type absorber	GaAs	Si	1×10^{18}	40	87
p-type absorber	GaAs	Be	1×10^{18}	40	
Electron barrier	In _{0.49} GaP	Be	5×10^{18}	20	19
p-type contact	GaAs	Be	1×10^{19}	25	25
Etch stop layer	InAlP	Be		150	145
Buffer	GaAs	Be		300	
Substrate	p-GaAs				

TABLE 1 Device layer structure as grown by molecular beam epitaxy

Note: This design is inverted during fabrication so that off wafer devices are p on n. Measured thicknesses are from ellipsometry (see the Supporting Information).

2 | DESIGN AND FABRICATION

Ultra-thin solar cells with an 80 nm GaAs pn junction were designed and fabricated with three different light management systems: on-wafer, rear surface planar Ag mirror and rear surface Ag/SiN nanophotonic diffraction grating. The epitaxial layer structure was grown as shown in Table 1 by molecular beam epitaxy (MBE). Layer thicknesses were measured using ellipsometry (see Supporting Information). Highly doped InGaP and InAlP were selected as passivating electron and hole barrier layers respectively, due to their favourable band alignments, while highly doped GaAs layers were included to form good Ohmic contacts. A thicker (300 nm) n-type contact layer was grown to allow an annealed Ni/AuGe/Ni/Au contact, without diffusing Au into the device active region. A non-annealed Ti/Au contact was used for the p-type contact.

Devices were processed with square 2.5 mm x 2.5 mm mesas. On-wafer devices were processed with an all front surface contacting scheme using a grid pattern with a contact pad on the top surface of the device for the n-type contact (10% shading loss) and a laterally displaced p-type contact outside the mesa area (Figure 1B). The front

surface contact layer was etched to reduce absorption. Off-wafer devices (planar Ag and nanophotonic) were processed with an inverted layer structure, employing the same front surface grid pattern as used for the on-wafer devices for the p-type contact and a rear surface grid (approx. 3.2% coverage) for the n-type contact. Both front and rear surface contact layers were etched.

In the case of the planar Ag devices, a layer of Ag was deposited by thermal evaporation directly onto the InAlP passivation layer. For the nanophotonic devices, 100 nm of SiN was first deposited by plasma-enhanced chemical vapour deposition and a hexagonal array of holes was patterned into the SiN using DTL and an inductively coupled plasma etch (Figure 1D). DTL operates by projecting the interference pattern of a periodic mask (illuminated by coherent light) onto a photosensitive resist. The interference pattern is three-dimensional and forms repeating self-images of the mask along the axis of incidence. The distance that separates consecutive self-images is called the Talbot period.¹³ The exposure step is carried out by displacing the wafer along the axis of incidence, normally by a few Talbot periods so that exposure uniformity is achieved along this axis in the resist and depth of field limitations are overcome.

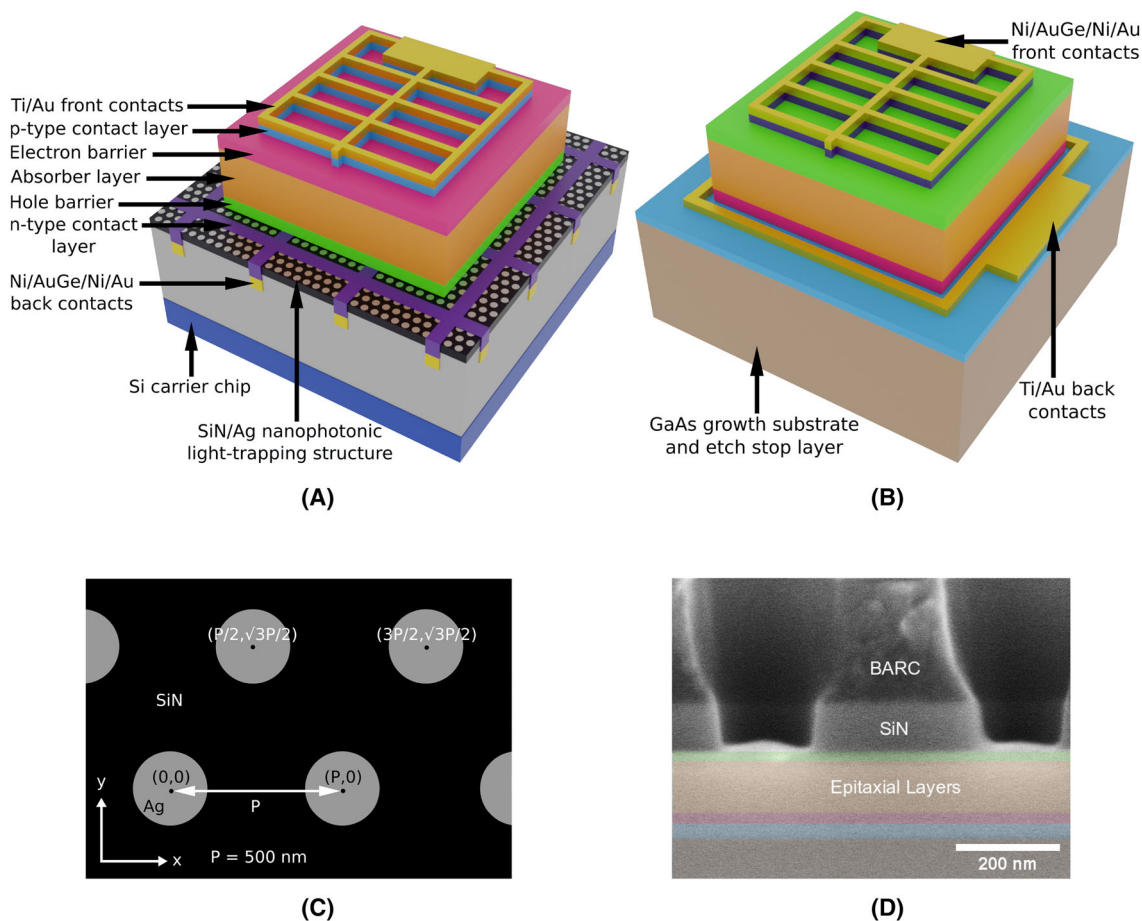


FIGURE 1 Diagram of 2.5 mm x 2.5 mm aperture devices: (A) processed with integrated nanophotonic light-trapping layer, (B) processed on wafer (lengths not to scale). (C) Unit cell diagram of the Ag/SiN hexagonal array. (D) Cross-sectional SEM image of the DTL patterned SiN, showing epitaxial layers, SiN and the bottom anti-reflective coating (BARC) used to enable precision patterning with DTL [Colour figure can be viewed at wileyonlinelibrary.com]

Rigorous coupled wave analysis (RCWA) was used to evaluate the optimal array geometry (pitch, Ag coverage and grating thickness) for the given device layer structure and process parameters were selected to fabricate an array which was as close as practically possible to this optimal. An array pitch of 500 nm was selected and exposure dose was adjusted to give circular features with average diameter 229 ± 24 nm (Figure 1C) and depth 80.5 ± 10.9 nm, leaving a SiN film of approximately 19.5 nm at the InAlP interface (see Methods for grating geometry evaluation). Ag was then evaporated over the perforated SiN layer similar to the planar Ag devices (Figure 1A).

Off-wafer devices were then bonded to a Si carrier using a high glassing temperature epoxy. They were then inverted and the substrate and subsequent etch stop layer were selectively etched to expose the GaAs p-type contact layer and enable front surface contacting (see Methods for further fabrication details).

3 | DEVICE PERFORMANCE

Device current-voltage characteristics were measured under a simulated AM0 spectrum (Figure 2A) (see Methods for measurement details). Both the off-wafer designs showed significant efficiency enhancement over the on-wafer equivalent, with the nanophotonic device providing the highest efficiency, 9.08% (no ARC and 10% shading loss) (Table 2). This performance enhancement was driven by an increase in J_{SC} (5.31 mA/cm^2) and an increase in V_{OC} (84 meV). J_{SC} is higher in the off-wafer devices as more charge carriers are photogenerated. Under open circuit conditions, this leads to an increase in charge carrier accumulation at the device terminals, corresponding to a higher V_{OC} . Using superposition, shifting the light IV curve of the on-wafer device to have J_{SC} matching that of the nanophotonic device, it is determined that this effect accounts for 28 meV of the observed difference in V_{OC} . The remaining 56 meV

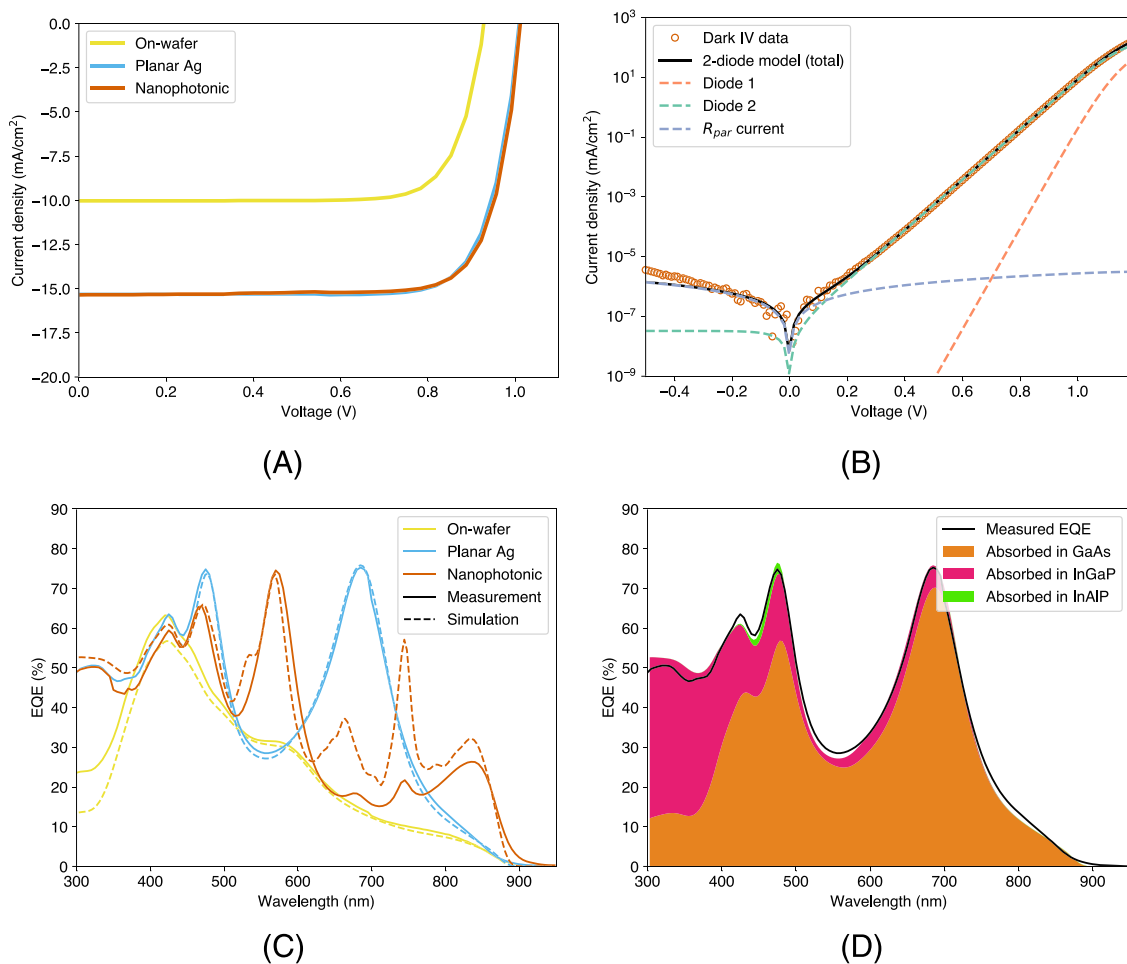


FIGURE 2 (A) Light IV characteristics under AM0 illumination for best performing on-wafer, planar Ag, and nanophotonic devices. (B) Dark IV characteristics of best performing nanophotonic device with 2-diode model fitting, showing the individual contributions to the current from the two diode terms and the shunt resistance (R_{par}).²⁰ (C) Simulated (dashed lines) and measured (solid lines) EQE of the three device types. (D) Calculated absorption in the GaAs, InGaP and InAlP layers of the planar Ag mirror device, compared to the measured EQE. The two off-wafer designs produce different EQE spectral features but their integrated EQE and corresponding J_{SC} is approximately the same. This leads to similar current-voltage characteristics as they have identical device structure [Colour figure can be viewed at wileyonlinelibrary.com]

TABLE 2 Light IV characteristics under an AM0 spectrum

Device	AM0 efficiency (%)	J_{sc} (mA/cm ²)	V_{oc} (V)	FF (%)
Nanophotonic	9.08	15.35	1.012	79.08
Planar Ag	9.06	15.33	1.010	79.22
On-wafer	5.40	10.04	0.928	78.41

Note: Devices have a 10% front surface shading loss and do not have any ARC.

TABLE 3 Dark IV data fitting parameters for the hero nanophotonic device compared to literature values

	Thickness (nm)		J_{01} (mA/cm ²)	J_{02} (mA/cm ²)	n_2	$R_{ser}(\Omega cm)^2$	$R_{par}(\Omega cm)^2$
	Total	Absorber					
Kayes et al. ³	~1000	-	6×10^{-18}	1×10^{-9}	2*	-	-
Chen et al. ¹⁰	330	205	2.8×10^{-17}	4.3×10^{-8}	2*	0.8	2.4×10^3
Hirst et al. ²	840	800	2.48×10^{-19}	7.71×10^{-9}	1.96	0.99	8.94×10^7
	120	80	1.74×10^{-18}	1.41×10^{-6}	2.70	13.23	3.77×10^6
This work	120	80	2.67×10^{-18}	3.29×10^{-8}	2.01	0.35	3.60×10^8

Note: The total thickness includes window and back surface field layers. * n_2 was held constant for these devices.

discrepancy, after superposition is considered, provides evidence of the fundamental voltage advantage afforded by light management. The off-wafer devices have higher charge carrier density in the ultra-thin device volume and this concentration factor further increases voltage.¹⁹

Current-voltage measurements were also acquired in the dark for the hero nanophotonic device (Figure 2B) and a 2-diode model was fitted²⁰ to extract diode performance parameters (saturation current densities J_{01} and J_{02} , series resistance R_{ser} and parallel resistance R_{par}). These are compared with equivalent literature results (Table 3). J_{02} is a measure of the recombination in the depletion region and therefore of particular interest for our fully depleted devices. A low value indicates good diode performance. In this work $J_{02}=3.29 \times 10^{-8}$ mA/cm² is measured. This is a significant improvement over a previously reported value ($J_{02}=1.41 \times 10^{-6}$ mA/cm²) for a comparable 80 nm device with Al_{0.3}Ga_{0.7}As passivation layers.² High J_{02} has also been reported for devices with 120 nm and 220 nm active layer thickness with AlGaAs passivation layers.^{4,21} This comparison indicates that surface passivation with InGaP and InAlP reduces depletion region recombination, allowing for enhanced performance in ultra-thin geometries. The value of J_{02} achieved here is comparable with results reported for devices which are >2.5 times as thick¹⁰; however, further reductions in J_{02} have been reported for devices which are an order of magnitude thicker.^{2,3} These much thicker devices are likely not fully depleted and therefore it is expected that surface effects will have less of an impact on J_{02} .

While the use of light management in ultra-thin geometries may give a fundamental boost in voltage, the higher J_{02} in these fully depleted devices will have the opposite effect, reducing FF and V_{oc} . It may be possible to iteratively improve device design to address this issue; however, achieving $V_{oc} > 1.1$ V as demonstrated by Kayes et al.³ will be challenging for devices on this length scale.

4 | OPTICAL PERFORMANCE

To evaluate optical performance, external quantum efficiency (EQE) was measured for the different light management designs (Figure 2C) (see Methods for experimental details). The on-wafer device exhibits low absorption at longer wavelengths where the absorption coefficient of GaAs is low. Long wavelength absorption is enhanced in both off-wafer designs, although different spectral features are observed. This can be attributed to an increasing optical path length. The off-wafer devices also exhibit enhanced absorption at short wavelengths (<400 nm). EQE in this wavelength range will be dominated by the front surface. The off-wafer devices have an inverted geometry, with InGaP on the front surface, while the on-wafer device has InAlP. The enhanced short wavelength EQE of the off-wafer devices indicates that self-passivation of the front surface InGaP is superior to that of InAlP, allowing charge carriers generated in this layer to be efficiently extracted as current (see Figure 2D). For this reason, the p-on-n orientation of the diode, as is the case for the off-wafer devices, is highly favourable for ultra-thin geometries. The enhanced absorption in the short wavelength regions also contributes towards the difference in measured J_{sc} under AM0 illumination and J_{sc} calculated from EQE for the best performing nanophotonic device (15.35 mA/cm² versus 14.68 mA/cm²). The integrated EQE underestimates the J_{sc} in part because EQE is high (>40%) at the calibration cut-off (300 nm) and also because the EQE illumination area is smaller than the device area, resulting in a larger fractional shading from the contact pad.

The EQE was analysed by comparing with RCWA simulations, transfer-matrix method (TMM) simulations, semi-analytical calculations of waveguide modes and analytical calculations of Fabry-Perot (FP) modes (see Methods). Waveguide modes arise due to constructive interference inside the device structure of waves which are diffracted by the grating and confined in the semiconductor film,

whereas Fabry-Perot modes arise due to light which is specularly reflected; for the device incorporating a diffraction grating, which is also highly reflective, we expect to see contributions from both effects. RCWA simulations incorporate both thin-film interference and diffraction effects, and can be used to compare to analytically calculated resonant wavelengths and the measured EQE. TMM simulations were used to model the performance of the planar devices (the on-wafer and planar Ag mirror devices) and to investigate the thin-film contributions in the device with a nanophotonic grating.

4.1 | Planar devices

The EQE was calculated from simulation by taking the combined absorption in the InGaP and GaAs layers, and assuming shading losses of 10% (Figure 2C). An excellent match is observed between the TMM simulations of the two planar devices and the measured EQE, indicating that almost all carriers generated in the GaAs and InGaP layers can be extracted. Figure 2D shows simulated absorption in the

front surface InGaP, GaAs junction and rear surface InAlP layers for the planar Ag device. This shows that absorption in the GaAs layer alone cannot account for the high EQE at short wavelengths, due to the significant absorption in the InGaP layer in the wavelength regime; 40% of 300 nm photons. Absorption in the InAlP is relatively low as this layer is positioned on the rear surface of the off-wafer devices. The sum of simulated photon absorption in the InGaP and GaAs layers gives a much better fit to the observed EQE indicating almost 100% carrier collection efficiency for charge carriers generated from the InGaP layer.

4.2 | Nanophotonic device

The measured EQE spectrum of a device with integrated rear surface nanophotonic structure is shown in Figure 2C alongside an RCWA simulation, showing good qualitative agreement. Multiple clear peaks are observed over the whole wavelength range; these spectral features, commonly referred to as resonances, result from wavelength

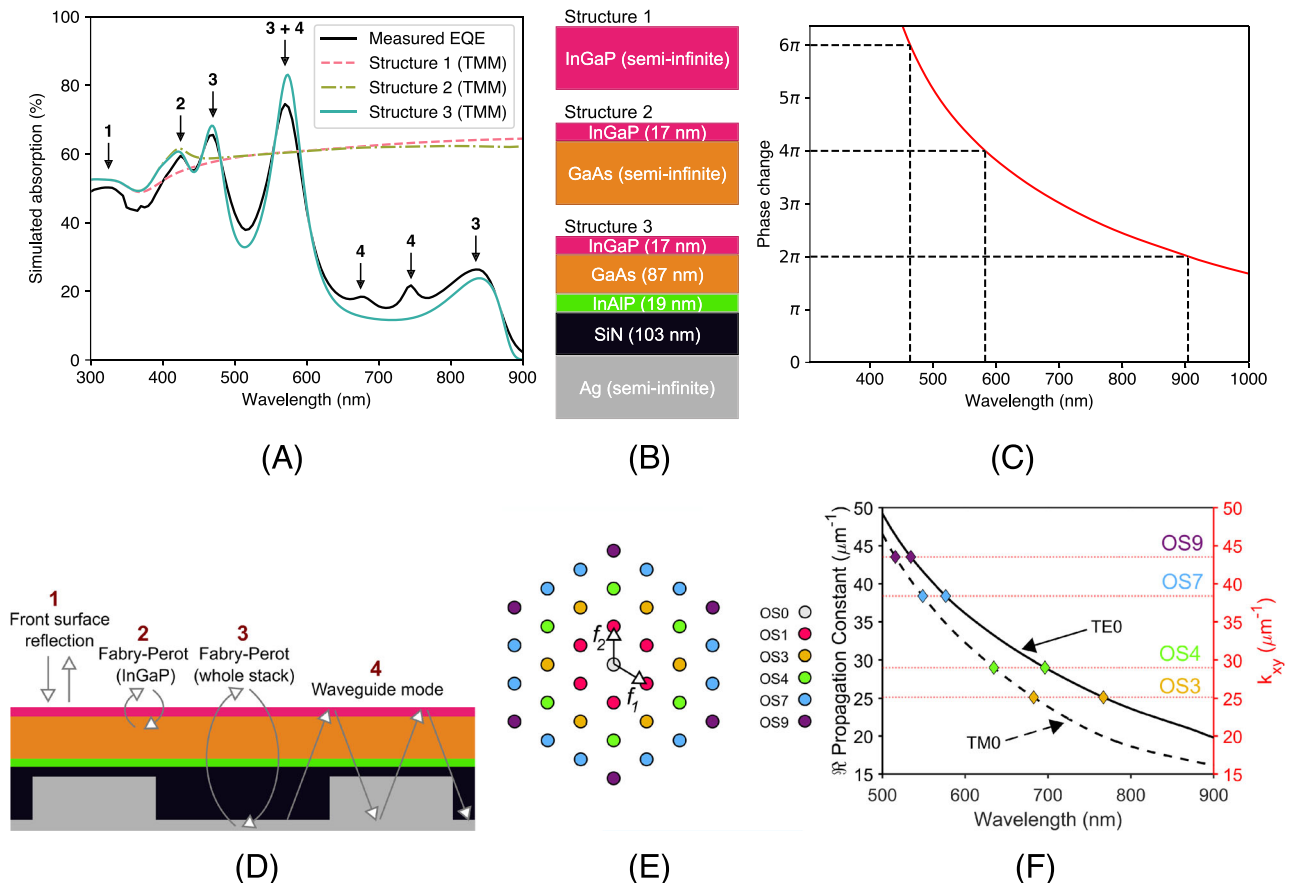


FIGURE 3 (A) Measured EQE for a device with the integrated nanophotonic structure with calculated values of $1 - R$ (total absorbed plus transmitted power) for the three simplified planar structures shown in part (B). Labeling of resonant peaks corresponds to the mechanisms illustrated in part (D). (B) Simplified planar structures used to identify different resonances. (C) For Structure 3, the phase change across the structure with wavelength (assuming light is trapped in the III-V layers and SiN and reflected by the Ag back mirror); this constructive interference leads to the peaks labelled (3) in part (A). (D) Field enhancement mechanisms corresponding to the observed peaks labelled in part (A). (E) Reciprocal space representation of the fabricated lattice in the grating, defining the allowed spatial frequencies for diffracted light in our devices. (F) Dispersion of the TE0 and TM0 modes in the fabricated devices. All possible coupling events to these modes at different sets of optical states (OS) are shown (see the Supporting Information for higher order modes) [Colour figure can be viewed at wileyonlinelibrary.com]

dependent enhancement of the E-field within the InGaP and GaAs layers, leading to an increased absorption of incident photons, and a corresponding increase in J_{SC} . Identifying the underlying physics responsible for these resonances is important in order to maximise any benefit, however, this not trivial as several different mechanisms contribute to the overall result. With a view to understanding the phenomena behind the EQE peaks in our nanophotonic devices, we consider two different optical effects: Fabry-Perot modes (thin-film effects) and waveguide modes.

With thin-film effects, the mechanism behind the E-field enhancement in the absorber is the constructive interference of incident and specularly reflected waves. The contributions made by specular reflection from different interfaces within the full structure can be inferred by simulating a series of simplified layer structures (Figure 3A). Values of $1 - R$ (total absorption) were calculated using TMM for three different planar structures (Figure 3B): a semi-infinite InGaP layer to study front surface reflection; a GaAs substrate with 17 nm of InGaP on top to study reflection at the InGaP/GaAs interface; and a full device structure with 103 nm SiN on the rear surface on a Ag substrate (i.e., the nanophotonic device structure without the silver disks). Comparison with the measured EQE shows that the short-wavelength feature below 400 nm can be explained as being purely due to reflection at the InGaP/air interface; since the light is absorbed very quickly inside the structure at such short wavelength, interference effects in the thin layers are not important. The feature around 425 nm can be explained by interference in the InGaP layer. The longer-wavelength features around 470, 570, and 835 nm can all be explained as Fabry-Perot (FP) modes in the stack made of the III-V layers and planar SiN layer; the condition for constructive interference in a specific set of layers can be calculated through:

$$2 \sum_i k_{z,i} d_i + \varphi_{fb} = 2\pi m \quad (1)$$

$$\varphi_{fb} = \varphi_{front} + \varphi_{back} = \angle r_{front} + \angle r_{back}$$

where m is any integer, $k_{z,i} = 2\pi n_i / \lambda$ is the z-component of the wavevector (for normal incidence) in layer i with refractive index n_i , d_i is the thickness of layer i and φ_{fb} is the additional phase change due to reflection at the front and back surface, which can be worked out from the Fresnel equations; r_{front} and r_{back} are the Fresnel reflection coefficients, evaluated with the appropriate complex refractive indices n_1 and n_2 ; for r_{front} , n_1 describes the incidence medium (air) and n_2 describes the first layer of the stack (InGaP), and for r_{back} the n_1 value is for the final layer in the stack (SiN) and n_2 describes the substrate (Ag). The symbol \angle denotes the phase of the complex number. Figure 3C shows the phase change across the cell structure, assuming modes can exist in the III-V layers plus SiN in between the Ag disks. The first three Fabry-Perot resonances in this cavity, corresponding to phase changes of 2π , 4π and 6π across the structure, occur at 904 nm, 582 nm, and 463 nm, respectively. The latter two wavelengths match extremely well with peaks observed in the EQE (at 570 nm and 470 nm). The long-wavelength peak in the EQE occurs at 835 nm, so below the predicted peak for the FP resonance; this is

likely due to the absorption edge of the GaAs causing the peak in absorbed power to occur below the resonant wavelength. The absorption profile calculated for Structure 3 (Figure 3B) shows a clear peak around 835 nm, confirming that this feature is due to a thin-film effect. The peaks at 675 nm and 745 nm cannot be explained by thin-film interference, even when different possible thin-film cavities in the structure were considered (see the Supporting Information) and were attributed instead to waveguide modes.

In waveguide modes, the field enhancement mechanism is the constructive interference of incident waves that are diffracted by the grating and propagate within the device as a result of total internal reflection. Under such conditions, phase changes are introduced in the wave as a result of its propagation and reflection at the interfaces in the device. Constructive interference then requires that all points on the same phase front of the propagating wave remain in phase. This condition restricts the occurrence of waveguiding to only a discrete set of propagating waves with specific in-plane wavevector components (k_{xy}), more commonly referred to as propagation constants. For a given wavelength, each propagation constant will correspond to a different waveguide mode, having a characteristic distribution of the electromagnetic field within the device.

We solve the propagation constants of the waveguide modes available in our fabricated devices by implementing a method for the waveguide analysis of multi-layered stacks.²² Using the experimentally determined thicknesses and optical constants and focusing on the spectral range between 500 and 900 nm, two modes are found to have a high field confinement in the active layer of the device (Supporting Information), one for each polarisation of light. Labelled TE0 and TM0, the high field confinement of these modes makes them more advantageous for absorption enhancement in the active layer. In our devices, coupling incident photons to these waveguide modes has a stringent dependence on the unit cell and

TABLE 4 Location of peaks in the measured EQE of the device with Ag/SiN grating, and their attribution to either waveguide modes arising from diffraction at the grating or Fabry-Perot (thin-film interference) modes

Peak location (nm)	Attribution	Calculated resonant wavelength (nm)
325	Air/InGaP reflection	312
425	Interference in InGaP	424
470	FP mode 2π phase change	463
570	Waveguide mode TE0@OS7	577 (Waveguide)
	+ FP mode 4π phase change	+ 582 (FP)
675	Waveguide modes TM0@OS3 / TE0@OS4	683 / 696
745	Waveguide mode TE0@OS3	767
835	FP mode 6π phase change	

periodicity of the grating, since they introduce boundary conditions which restrict the allowed k_{xy} for diffracted light. In our fabricated devices with a hexagonal array of disks (pitch = Λ), the reciprocal lattice vectors are $f_1 = \frac{1}{\Lambda}\hat{x} - \frac{\sqrt{3}}{3\Lambda}\hat{y}$ and $f_2 = \frac{2}{\sqrt{3}\Lambda}\hat{y}$. For these conditions and considering normal light incidence, the allowed k_{xy} are defined by the following equation:

$$k_{xy} = \frac{4\pi}{\sqrt{3}\Lambda} \sqrt{m_1^2 - m_1 m_2 + m_2^2}, \quad (2)$$

where m_1 and m_2 are pairs of integers which define optical states. According to Equation (2), coupling to a waveguide mode at a given wavelength is enabled at an optical state when its corresponding k_{xy} matches the propagation constant of the mode (Figure 3F). Since different optical states may correspond to the same k_{xy} (and thus enable the same coupling event), we group these into sets and label them OSx (Figure 3E), with x being the value that all these states yield inside the square root in Equation (2).

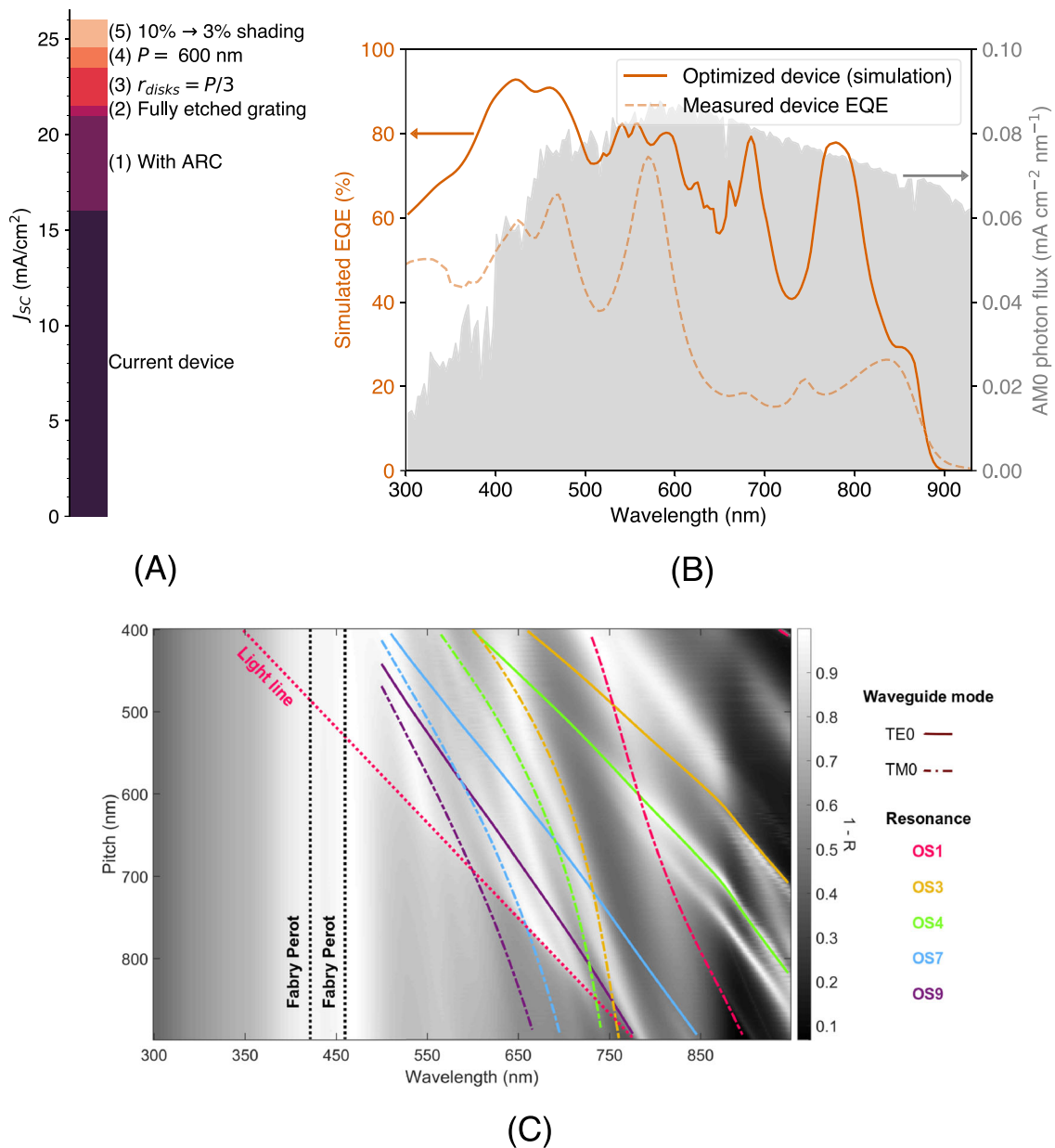


FIGURE 4 (A) Expected gain in the simulated short-circuit current J_{sc} for successive improvements to the nanophotonic device. (B) Simulated EQE for the device with all five improvements, as compared to the measured EQE of the fabricated device with nanophotonic grating and AMO photon flux. (C) Spectral dependence of simulated total absorption ($1 - R$, since the Ag substrate in the simulations is opaque), shown in the intensity plot, and waveguide modes (lines) as a function of grating pitch for the optimized cell design (70 nm Al_2O_3 , fully etched 100-nm-thick grating, disk radius $r=P/3$). Increasing pitch shifts waveguide modes to longer wavelengths, where GaAs is less absorbing. The light line (OS1) marks the limit at which diffracted power transitions from evanescent to propagating in air, with shorter wavelength light escaping the device at the front surface [Colour figure can be viewed at wileyonlinelibrary.com]

Equation (2) identifies waveguide modes as mechanisms behind the peaks at $\lambda = 570, 675$ and 745 nm in the EQE data (Table 4). The peak at $\lambda = 745$ nm is associated to coupling to the TE0 mode at OS3, whereas the one at $\lambda = 675$ nm has contributions from coupling to both TM0 at OS3 and TE0 at OS4. As for the peak at $\lambda = 570$ nm, this strong and broad resonance has contributions from TE0 coupling at OS7 together with the previously described thin-film effect. The differences between the predicted resonant wavelengths in Table 4 and those at which their associated EQE peaks are found are small (within $\sim 3\%$), but quantification of these discrepancies is limited in cases when more than one field enhancement mechanism is found in the vicinity of a peak. We attribute any discrepancies mainly to the effective medium approximation used to describe the grating in our method for waveguide analysis (accounting for the deviations in the measured grating thickness and disk radius did not change the calculated resonant wavelengths significantly, with variations staying below $\Delta\lambda = 10$ nm for all modes). Four other TE0 and TM0 coupling events can be predicted with Equation (2) within $\lambda = 515 - 635$ nm, and these are likely contained within the broad peak at 570 nm.

Finally, it can be seen in Figure 2C that the peaks in the measured EQE associated with coupling to waveguide modes are significantly higher in the equivalent RCWA simulation, indicating there is some discrepancy between simulated and observed diffraction effects. As can be seen in Figure 1D, the real structures were not exactly as simulated, with the bottom of the etched holes not being perfectly flat and with some tapering of the walls of the etched holes. Not all holes in the SiN were etched to exactly the same depth, and some holes were not perfectly circular or were missing altogether (see the Supporting Information for top-view SEM images of the nanophotonic grating). In addition, some residual BARC remained after plasma etching. These irregularities may affect the diffraction efficiency of the grating, leading to lower EQE contributions from waveguide modes.

5 | FUTURE PERFORMANCE ENHANCEMENTS

Five potential methods for improving the J_{SC} of the devices, which are possible without altering the device fabrication steps or DTL process significantly, are evaluated (Figure 4A): (i) addition of an ARC, (ii) full etching of the SiN layer, (iii) optimizing disk radius, (iv) optimizing grating pitch and (v) reducing front contact shading losses. These theoretical increases in the J_{SC} are calculated assuming that all of these improvements are applied sequentially, but any one of these improvements could be made in isolation. The currents were calculated using RCWA simulations.

The first possible improvement, increasing the simulated current by almost one third, is the addition of a simple single-layer ARC (70 nm of Al_2O_3). This reduces reflection from the front surface, allowing more light to enter the cell; simulations indicated that 70 nm of Al_2O_3 performed optimally for a range of devices with and without all

the improvements discussed here, and performed as well as an optimized double-layer MgF_2/Ta_2O_5 ARC (see Supporting Information). Improvements (ii)-(iv) relate to the dimensions of the grating; without changing the mask used to produce the grating or the epitaxial layer structure, the current could be improved by 3% by ensuring that the grating disks are etched all the way through the SiN layer. RCWA simulations exploring the design space of similar gratings for ultra-thin GaAs cells²³ have shown that absorption in the GaAs can be improved further by tuning the pitch and disk size of the hexagonal grating (assuming the same materials, SiN and Ag, are used, and the same type of DTL mask leading to a hexagonal array of circular disks). The disk size in the current embodiment is lower than the optimum value predicted by simulations, which indicate that a disk radius close to one third of the grating pitch gives optimal absorption enhancement. Increasing the disk radius in the simulations from 114.5 nm to 160 nm shows an increase to the current of 9%. This change could be achieved by increasing the exposure dose used for the DTL patterning. If a different DTL mask is used, the pitch of the disks can be changed; the optimum is expected to lie between 600-700 nm for this cell thickness and grating symmetry. Increasing the pitch pushes the waveguide modes to longer wavelengths (Figure 4C). This will also increase the wavelength below which diffracted modes can escape the front surface (light line), however, at $\lambda = 600$ nm this occurs at $\lambda = 500$ nm. Below this wavelength the GaAs layer will be highly absorbing on a single pass and therefore current loss from diffracted light escaping the front surface will be minimal. Changing the pitch of the grating to 600 nm, and keeping the disk radius at one third of the grating pitch gives a further current improvement of 3% (it was found that for any given pitch, the optimal disk size lies close to one-third of the pitch, as was the case for the 500 nm grating). Finally, an obvious potential improvement to the current can be made by reducing the contact shading; in these devices, the contact shading was estimated at 10%, but this could be reduced to $<3\%$,^{24,25} without impacting on charge carrier collection efficiency. Figure 4B shows the simulated EQE of the device with all the improvements discussed, as compared to the EQE of the fabricated device with nanophotonic grating.

These improvements could increase the J_{SC} for the nanophotonic device from 15.35 mA/cm² to 26.0 mA/cm²; assuming superposition of the current-voltage characteristics of our measured devices, this gives solar energy conversion efficiency 16.0%. For comparison, the J_{SC} of the planar Ag and on-wafer devices could be improved to 21.8 mA/cm² and 15.1 mA/cm² respectively, applying the same ARC and

TABLE 5 Comparison of measured J_{SC} and efficiency for hero nanophotonic, planar Ag and on-wafer devices, with simulated improvements

Device type	$J_{SC}(\text{mA}/\text{cm}^2)$		efficiency (%)	
	measured	improved	measured	improved
nanophotonic	15.35	26.0	9.08	16.0
planar Ag	15.33	21.8	9.06	14.0
on-wafer	10.04	15.1	5.40	9.5

also assuming 3% contact shading. The nanophotonic light management system therefore has the greatest potential for high current and high solar energy conversion efficiency for this device geometry (Table 5).

6 | CONCLUSIONS

In this work solar energy conversion efficiency enhancement in ultra-thin GaAs solar cells (80 nm absorber thickness) is demonstrated using nanophotonic integration. Intrinsic radiation tolerance that has previously been demonstrated on this length scale is sufficient to enable new mission types in hostile environments as well as lightweight flexible form factors by reducing or eliminating the need for protective coverglass; however, the ultra-thin absorbers are highly transmissive and require integrated light management to increase current.

The use of displacement Talbot lithography to fabricate a metal/dielectric hexagonal nanophotonic array is demonstrated. This technique is inherently suited to wafer-scale, high throughput fabrication and therefore a feasible approach for manufacturing large area photovoltaic devices with integrated light management. The performance of a device with a rear surface Ag/SiN nanophotonic grating is compared to that of a device with a rear surface planar Ag mirror and a device processed on-wafer. Both off-wafer embodiments had higher J_{SC} and V_{OC} than the on-wafer equivalent, with the nanophotonic device demonstrating the highest efficiency, 9.08% (AM0, no ARC, 10% shading loss), a 68% improvement in efficiency relative to the on-wafer device.

EQE measurements show enhanced current in the off-wafer designs at short and long wavelengths. The short wavelength enhancement is attributed to the superior performance of InGaP as a front surface passivation layer, with simulations confirming near 100% carrier collection efficiency of photogenerated charge carriers in this layer. In the near infra-red region of the spectrum, high EQE is attributed to light trapping effects. For the nanophotonic device, simulations confirm absorption contributions from both Fabry-Perot resonances due to specular reflection at different interfaces within the structure, and light diffracted at the rear surface nanophotonic structure coupling to waveguide modes.

It was determined using simulation that the integration of an ARC and reduction in front surface grid contact shading could improve efficiency of the on-wafer and planar Ag devices to 9.5% and 14.0% respectively. These same adaptations, in addition to optimization of the grating geometry, would enable efficiency of 16.0% in the nanophotonic device. Simulations show that increasing the pitch of the nanophotonic grating shifts waveguide resonances to longer wavelengths, where GaAs is less absorbing, allowing for an increase in J_{SC} . The proposed improvements could be implemented without significant changes to the device and grating fabrication process. These results show that future embodiments of ultra-thin devices are unlikely to complete with current industry standard multijunction photovoltaics on efficiency alone, however, the potential efficiency gains of nanophotonic integration demonstrated here, alongside low mass

and inherent radiation tolerance, might enable new mission profiles and launch cost reductions, making ultra-thin devices a compelling platform for development.

7 | METHODS

7.1 | Step-by-step process flow

Devices were fabricated using the following step-by-step process flow.

- Nanophotonic device: n-type contact, DTL, Ag mirror, bond and etch, p-type contact and mesa etch
- Planar Ag device: n-type contact, Ag mirror, bond and etch, p-type contact and mesa etch
- On-wafer device: mesa etch, n-type contact, p-type contact, n-type contact etch

7.2 | n-type contact metalisation

Metal contacts were deposited via thermal evaporation and lift-off. The n-type contact was annealed Ni/AuGe/Ni/Au (10/135/30/200 nm). The anneal was 20 seconds at 350°C. The time and temperature were kept to a minimum to avoid large amounts of Au diffusion into the active layers of the cell which can decrease shunt resistance. This is an issue that is specific to the ultra-thin geometry and was optimised using transmission line measurement studies of the contacts at various anneal conditions. The exposed n-type contact layer regions were then etched away using a selective 2:1:10, $\text{NH}_4\text{OH}:\text{H}_2\text{O}_2:\text{H}_2\text{O}$ etchant.

7.3 | p-type contact metalisation

Ti/Au (20/200 nm) p-type contacts were deposited using thermal evaporation and lift-off. In the case of the off-wafer devices the exposed p-type contact layer was then etched away using a selective 2:1:10, $\text{NH}_4\text{OH}:\text{H}_2\text{O}_2:\text{H}_2\text{O}$ etchant.

7.4 | Mesa etch

Photolithography was used to protect the device areas (2.5 mm × 2.5 mm) and devices were isolated by selectively etching back the layered structure by alternating between concentrated HCl and 2:1:10 $\text{NH}_4\text{OH}:\text{H}_2\text{O}_2:\text{H}_2\text{O}$ etchant until the Ag back mirror was exposed.

7.5 | Ag mirror evaporation, bonding, and wafer etching

A total of 12 mm x 12 mm square sections of an Ag back mirror were thermally evaporated onto the wafer at a thickness of 450 nm. These

square sections were cleaved and bonded to Si carrier chips using OPT5054-4G two-part Optitec epoxy. Each square of Ag produced 9 devices. The epoxy was cured for 30 minutes at 120°C. The substrate was etched back using a 1:10, NH₄OH:H₂O₂ etchant. The etch stop layer was removed with concentrated HCl.

7.6 | Displacement Talbot lithography

The rear surface nanophotonic structure grating was patterned using displacement Talbot lithography. First, a SiN layer (100 nm nominal thickness) was deposited using plasma-enhanced chemical vapour deposition. Then a bottom anti-reflection coating (BARC) (Wide 30 W - Brewer Science) was spin coated on the wafer (two-cycle process, 5 s at 500 rpm + 30 s at 3000 rpm). This process was followed by two baking steps (80°C for 60 s + 200°C for 90 s) to yield a BARC thickness of ~250 nm. Afterwards, a positive resist (PFI-88, Sumitomo Chemical Co.) was spin coated on the BARC (same two-cycle process as used for the BARC) followed by a baking step (90 s at 90°C) to yield a thickness ~750 nm. The wafer was then exposed with DTL (PhableR 100, Eulitha), using a mask with circular openings (diameter = 300 nm) arranged in a hexagonal array with 500 nm pitch (Talbot period of the mask = 750 nm). The exposure was carried out using a displacement of 20 Talbot periods, with an initial gap between mask and wafer ~100 μm, and using a 375 nm laser. The exposure dose was 55 mJ/cm². Following the exposure, a post-baking step was carried out (90 s at 120°C) and the resist developed (using MF-CD-26 for 90 s). The wafer with the developed resist was then etched with an inductively coupled plasma (ICP) dry etch system (Oxford Instruments System 100 Cobra) (550 s at 25 sccm CHF₃, 300 W ICP power, 50 W RIE power, 6.5 mTorr, 20°C). Cross-sectional scanning electron microscopy (SEM) images of the result of this etching process (Figure 1D) show a good anisotropy in the etched holes, which are also seen to contain thin, dome-shaped regions of unetched SiN at the bottom. Further etching to remove these regions was not attempted in order to preserve the underlying 20 nm InAlP layer. Following the etching process, the remaining resist was removed by exposing the full wafer to the 375 nm laser at a power of 2 mW/cm² for 2 min. The exposed resist was then developed and the wafer rinsed with acetone and IPA. The BARC layer was removed by putting the wafer under a gentle O₂ plasma.

7.7 | Determination of disk size and grating thickness

In order to determine the size of the disks in the grating, ~1 cm² chips were cleaved from the perimeter of the wafer processed with DTL, after etching the holes in the SiN layer and prior to the Ag evaporation. Images of the chips were acquired with scanning electron microscopy (SEM) and studied with a MATLAB-based Hough transform algorithm to detect and measure the etched holes. Such studies revealed an average hole diameter of 229 ± 24 nm (for a total of 9169 holes).

To estimate the depth of the etched holes in the SiN layer, atomic force microscopy measurements were done on the same chips cleaved from the processed wafer. The topography measurements revealed the presence of residual SiN 'domes' at the bottom of the etched holes, in agreement with our cross-sectional SEM images. Since most holes presented these domes at the bottom, the etch depth was measured from the top of such domes to the neighbouring SiN surface at the top of the holes. Data from 125 holes gave an average hole depth of 80.5 ± 10.9 nm.

7.8 | Device testing

EQE measurements were conducted at zero volts without bias light using a Bentham PVE300 system, calibrated with a Si photodiode (NMI traceable). A 1.5 mm by 1.5 mm spot size was used. Light IV measurements were conducted under a simulated AM0 spectrum using a TS Space Systems Unisim Compact. This dual source system was calibrated using a spectrophotometer. Cell temperature was fixed at 25°C.

7.9 | EQE simulations

EQE was calculated by simulating absorption in the GaAs and InGaP layers and assuming a uniform 10% shading loss due to the front contacts. It was assumed all charge carriers generated in these layers were collected (100% internal quantum efficiency). Absorption in all other layers was assumed to be parasitic. Layer thicknesses and optical constants for all deposited materials (the III-V materials, SiN, and Al₂O₃) were evaluated using ellipsometry measurements (see Supporting Information), with the exception of silver, data for which was taken from the crystal monitor of the thermal evaporator and from reference.²⁶ The transfer matrix method (TMM), as included in the modular solar simulation package Solcore,²⁷ was used to simulate the performance of the two types of planar device (the on-wafer device and the device with the planar Ag rear surface mirror), showing excellent agreement between the measured EQE and simulated EQE. The nanophotonic device performance was simulated using a modified version of S⁴ (see Supporting Information for further details) to perform RCWA simulations,²⁸ in conjunction with RayFlare²⁹ which provides convenient functions for defining structures and handling layers with varying optical constants, as well as processing the results of S⁴ into useful quantities for PV applications such as absorption per layer. The total thickness of the SiN layer prior to etching the grating was 103 nm, measured through ellipsometry. The grating was modelled as two separate layers: a 22.5 nm layer of planar SiN below the InAlP layer, which accounts for the SiN not being fully etched through, and an 80.5 nm layer of SiN with silver disks arranged as in Figure 1C. The RCWA results in Figures 2C, 2D and 4C were all generated using 235 Fourier orders chosen using circular lattice truncation rules. Further details of the settings used in the RCWA simulations are given in the Supporting Information.

7.10 | Modal analysis

The calculation of the waveguide modes was done by implementing a transfer matrix method for the waveguide analysis of multi-layered planar stacks.^{22,30} This method takes as input the thicknesses and complex refractive indices of all the layers in the stack. In our implementation, the grating is represented as a uniform slab having an effective index corresponding to the average of its component materials weighted by their volume ratio within the unit cell. The outputs of the transfer matrix method are dispersion equations for TE and TM polarisation, whose roots correspond to the propagation constants of the available waveguide modes. We find these roots following a Newton-Raphson method in the complex plane.

ACKNOWLEDGEMENTS

This study is supported by the H2020 European Research Council, Grant/Award Number: 853365; UK Space Agency, Grant/Award Number: PF2-012; Engineering and Physical Sciences Research Council, Grant/Award Number: EP/L015978/1, EP/M015181/1 and EP/M022862/1; Consejo Nacional de Ciencia y Tecnología; Cambridge Trust; the Isaac Newton Trust.

DATA AVAILABILITY STATEMENT

The data that support the findings of this study are available from the corresponding author upon reasonable request.

ORCID

Larkin Sayre  <https://orcid.org/0000-0002-1768-8396>

Eduardo Camarillo Abad  <https://orcid.org/0000-0001-8617-0059>

Phoebe Pearce  <https://orcid.org/0000-0001-9082-9506>

Pierre-Marie Coulon  <https://orcid.org/0000-0002-9120-7554>

Philip Shields  <https://orcid.org/0000-0003-0517-132X>

Louise C. Hirst  <https://orcid.org/0000-0003-0073-6344>

REFERENCES

- Massiot I, Cattoni A, Collin S. Progress and prospects for ultrathin solar cells. *Nat Energy*. 2020;5(12):959-972. <https://doi.org/10.1038/s41560-020-00714-4>
- Hirst LC, Yakes MK, Warner JH, et al. Intrinsic radiation tolerance of ultra-thin GaAs solar cells. *Appl Phys Lett*. 2016;109(3):033908. <https://doi.org/10.1063/1.4959784>
- Kayes BM, Nie H, Twist R, et al. 27.6% Conversion efficiency, a new record for single-junction solar cells under 1 sun illumination. In: *2011 37th IEEE Photovoltaic Specialists Conference*; 2011 000004-000008.
- Vandamme N, Chen H, Gaucher A, et al. Ultrathin GaAs solar cells with a silver back mirror. *IEEE J Photovolt*. 2015;5(2):565-570. <https://doi.org/10.1109/JPHOTOV.2014.2371236>
- Yang W, Becker J, Liu S, et al. Ultra-thin GaAs single-junction solar cells integrated with a reflective back scattering layer. *J Appl Phys*. 2014;115(20):203105. <https://doi.org/10.1063/1.4878156>
- Shoji Y, Watanabe K, Okada Y. Photoabsorption improvement in multi-stacked InGaAs/GaAs quantum dot solar cell with a light scattering rear texture. *Solar Energy Mater Solar Cells*. 2020;204:110216. <https://doi.org/10.1016/j.solmat.2019.110216>
- Eerden VM, Bauhuis GJ, Mulder P, et al. A facile light-trapping approach for ultrathin GaAs solar cells using wet chemical etching. *Prog Photovolt Res Appl*. 2020;28(3):200-209. <https://doi.org/10.1002/pip.3220>
- D'Rozario JR, Polly SJ, Nelson GT, Hubbard SM. Thin gallium arsenide solar cells with maskless back surface reflectors. *IEEE J Photovolt*. 2020;10(6):1681-1688. <https://doi.org/10.1109/JPHOTOV.2020.3019950>
- Grandier J, Callahan DM, Munday JN, Atwater HA. Gallium arsenide solar cell absorption enhancement using whispering gallery modes of dielectric nanospheres. *IEEE J Photovolt*. 2012;2(2):123-128. <https://doi.org/10.1109/JPHOTOV.2011.2180512>
- Chen HL, Cattoni A, de Lépinay R, et al. A 19.9%-efficient ultrathin solar cell based on a 205-nm-thick GaAs absorber and a silver nanostructured back mirror. *Nat Energy*. 2019;4(September):761-767. <https://doi.org/10.1038/s41560-019-0434-y>
- Lee SM, Kwong A, Jung D, et al. High performance ultrathin GaAs solar cells enabled with heterogeneously integrated dielectric periodic nanostructures. *ACS Nano*. 2015;9(10):10356-10365. <https://doi.org/10.1021/acsnano.5b05585>
- Coulon PM, Damilano B, Alloing B, et al. Displacement Talbot lithography for nano-engineering of III-nitride materials. *Microsyst Nanoeng*. 2019;5(1):1-12. <https://doi.org/10.1038/s41378-019-0101-2>
- Solak HH, Dais C, Clube F. Displacement Talbot lithography: a new method for high-resolution patterning of large areas. *Opt Express*. 2011;19(11):10686-10691. <https://doi.org/10.1364/OE.19.010686>
- Chausse P, Boulbar EL, Coulon PM, Shields PA. "Double" displacement Talbot lithography: fast, wafer-scale, direct-writing of complex periodic nanopatterns. *Opt Express*. 2019;27(22):32037-32046. <https://doi.org/10.1364/OE.27.032037>
- Brongersma ML, Cui Y, Fan S. Light management for photovoltaics using high-index nanostructures. *Nat Mater*. 2014;13(5):451-460. <https://doi.org/10.1038/nmat3921>
- Green MA, Pillai S. Harnessing plasmonics for solar cells. *Nature Photon*. 2012;6(3):130-132. <https://doi.org/10.1038/nphoton.2012.30>
- Massiot I, Vandamme N, Bardou N, et al. Metal nanogrid for broadband multiresonant light-harvesting in ultrathin GaAs layers. *Acs Photon*. 2014;1(9):878-884. <https://doi.org/10.1021/ph500168b>
- Hirst L. Ever thinner high-efficiency cells. *Nat Energy*. 2019;4(9):726-727. <https://doi.org/10.1038/s41560-019-0444-9>
- Miller OD, Yablonovitch E, Kurtz SR. Strong internal and external luminescence as solar cells approach the Shockley-Queisser Limit. *IEEE J Photovolt*. 2012;2(3):303-311. <https://doi.org/10.1109/JPHOTOV.2012.2198434>
- Suckow S. 2/3 Diode Fit. 2014. <http://nanohub.org/resources/14300>
- Vandamme N. Nanostructured ultrathin GaAs solar cells. PhD thesis. Université Paris Sud, Paris XI. 2015.
- Camarillo Abad E, Joyce HJ, Hirst LC. Light management in ultra-thin solar cells: a guided optimisation approach. *Opt Express*. 2020;28(26):39093-39111. <https://doi.org/10.1364/OE.408664>
- Pearce P, Sayre L, Johnson A, Hirst L, Ekins-Daukes NJ. Design of photonic light-trapping structures for ultra-thin solar cells. In: Freundlich A, Sugiyama M, Collin S, eds. *Physics, Simulation, and Photonic Engineering of Photovoltaic Devices IX*; 2020:28.
- Bauhuis G, Mulder P, Haverkamp E, Huijben J, Schermer J. 26.1% thin-film GaAs solar cell using epitaxial lift-off. *Solar Energy Mater Solar Cells*. 2009;93(9):1488-1491. <https://doi.org/10.1016/j.solmat.2009.03.027>
- Gruginskie N, Cappelluti F, Bauhuis G, et al. Limiting mechanisms for photon recycling in thin-film GaAs solar cells. *Prog Photovolt Res Appl*. 2021;29(3):379-390. <https://doi.org/10.1002/pip.3378>

26. Jiang Y, Pillai S, Green MA. Realistic silver optical constants for plasmonics. *Sci Rep*. 2016;6(1):30605. <https://doi.org/10.1038/srep30605>
27. Alonso-Álvarez D, Wilson T, Pearce P, Führer M, Farrell D, Ekins-Daukes N. Solcore: a multi-scale, Python-based library for modelling solar cells and semiconductor materials. *J Comput Electron*. 2018;17(3):1099-1123. <https://doi.org/10.1007/s10825-018-1171-3>
28. Liu V, Fan S. S4: A free electromagnetic solver for layered periodic structures. *Comput Phys Commun*. 2012;183(10):2233-2244. <https://doi.org/10.1016/j.cpc.2012.04.026>
29. Pearce P, Ekins-Daukes N. Open-source integrated optical modelling with RayFlare. In: *2019 IEEE 46th Photovoltaic Specialists Conference (PVSC)*; 2019:2627-2633.
30. Chen C, Berini P, Feng D, Tanev S, Tzolov VP. Efficient and accurate numerical analysis of multilayer planar optical waveguides in lossy anisotropic media. *Opt Express*. 2000;7(8):260-272.

SUPPORTING INFORMATION

Additional supporting information may be found in the online version of the article at the publisher's website.

How to cite this article: Sayre L, Camarillo Abad E, Pearce P, et al. Ultra-thin GaAs solar cells with nanophotonic metal-dielectric diffraction gratings fabricated with displacement Talbot lithography. *Prog Photovolt Res Appl*. 2021;1-13. doi: 10.1002/pip.3463